HHS Public Access

Author manuscript

Endocr Relat Cancer. Author manuscript; available in PMC 2021 October 01.

Published in final edited form as:

Endocr Relat Cancer. 2020 October ; 27(10): 529–539. doi:10.1530/ERC-20-0295.

Real-time, high-resolution imaging of tumor cells in genetically engineered and orthotopic models of thyroid cancer

Xhesika Shanja-Grabarz, MD[1,*], **Anouchka Coste, MD**[2,*], **David Entenberg, PhD**[2], **Antonio Di Cristofano, PhD**[1]

[1]Department of Developmental and Molecular Biology, Albert Einstein College of Medicine / Montefiore Medical Center, Bronx, New York.

[2]Department of Anatomy and Structural Biology, Albert Einstein College of Medicine / Montefiore Medical Center, Bronx, New York.

Abstract

Genetically engineered and orthotopic xenograft mouse models have been instrumental for increasing our understanding of thyroid cancer progression and for the development of novel therapeutic approaches in a setting that is more physiologically relevant than the classical subcutaneous flank implants. However, the anatomical location of the thyroid gland precludes a non-invasive analysis at the cellular level of the interactions between tumor cells and the surrounding microenvironment and does not allow a real-time evaluation of the response of tumor cells to drug treatments. As a consequence, such studies have generally only relied on endpoint approaches, limiting the amount and depth of the information that could be gathered.

Here we describe the development of an innovative approach to imaging specific aspects of thyroid cancer biology, based on the implantation of a permanent, minimally invasive optical window that allows high-resolution, multi-day, intravital imaging of the behavior and cellular dynamics of thyroid tumors in the mouse.

We show that this technology allows visualization of fluorescently tagged tumor cells both in immunocompetent, genetically engineered mouse models of anaplastic thyroid cancer (ATC), and in immunocompromised mice carrying orthotopic implanted human or mouse ATC cells. Furthermore, the use of recipient mice in which endothelial cells and macrophages are fluorescently labeled allows the detection of the spatial and functional relationship between tumor cells and their microenvironment. Finally, we show that ATC cells expressing a fluorescent biosensor for caspase 3 activity can be effectively utilized to evaluate in real time the efficacy and kinetics of action of novel small molecule therapeutics.

Corresponding authors: A. Di Cristofano, Department of Developmental and Molecular Biology, Albert Einstein College of Medicine, 1301 Morris Park Avenue, Room 302, Bronx, NY 10461. Tel: 718-678-1137; antonio.dicristofano@einsteinmed.org.; **D. Entenberg**, Department of Anatomy and Structural Biology, Albert Einstein College of Medicine, Bronx, New York, 1301 Morris Park Avenue, Room 202, Bronx, NY 10461. Tel: 718-678-1116; david.entenberg@einsteinmed.org.

*equal contribution

AUTHORS DISCLOSURE STATEMENT

The authors have nothing to disclose.

This novel approach to intravital imaging of thyroid cancer represents a platform that will allow, for the first time, the longitudinal, in situ analysis of tumor cell responses to therapy, and of their interaction with the microenvironment.

Keywords

Imaging; thyroid cancer; mouse models; high-resolution; apoptosis

INTRODUCTION

Intravital multiphoton microscopy has emerged as an important technique to study pathogenetic events in a live animal model that closely recapitulates human disease (Coste et al., 2019). This technology allows the study of a diverse set of biological and clinical parameters, including the kinetics of tumor cell infiltration and migration, the vascular remodeling induced by tumor growth, and the recruitment of cells into the tumor microenvironment. As such, it has yielded a great deal of information about primary breast cancer tumor biology (Ke et al., 2013), the nature of the metastatic niche (Schaefer et al., 2011, Ritsma et al., 2012), and the behavior of tumor-associated macrophages (Chen et al., 2019). The method has also been adapted to study a wide variety of non-neoplastic diseases including those of liver, kidney and pancreas (Malehmir et al., 2019, Gyarmati et al., 2018, Lehmann et al., 2016).

An additional critical area of application of intravital imaging is represented by the study of the mechanism and efficacy of anti-tumor and anti-angiogenic drugs. Although significant advancements have been made in recent years in utilizing our increased knowledge of tumor biology to develop targeted therapies for a wide variety of solid cancers (Baudino, 2015), there are limited data that show how these drugs actually work in vivo. The differences between drug effects observed in vitro and those obtained in vivo are often associated with both drug pharmacokinetics and the activity of the tumor microenvironment (Saeidnia et al., 2015, Wu and Dai, 2017, Hui and Chen, 2015). In fact, intravital imaging has been successfully employed, for example, to identify tumor-associated macrophages as the target of bisphosphonate in breast cancer (Junankar et al., 2015), to track drug response in the hypoxic regions of pancreatic cancer (Conway et al., 2018), and to monitor the efficacy of cytotoxic drugs in pancreatic cancer (Vennin et al., 2017).

To date, no intravital imaging approaches have been described for the analysis of thyroid cancer models.

Poorly differentiated and anaplastic thyroid cancer are extremely difficult to treat despite the development of novel promising therapeutics (Saini et al., 2018). This is at least in part due to the fact that they are characteristically driven by multiple mutations and exhibit a large degree of genome complexity (Xu et al., 2020, Landa et al., 2016). Furthermore, many aspects of the in vivo biology of these tumors are still obscure.

We sought to develop a novel intravital imaging approach to study thyroid cancer biology and therapeutic response in vivo, which would potentially allow, for the first time, evaluation

of the tumor architecture in different murine models, the composition and dynamics of the tumor microenvironment, and the visualization of drug effects in vivo using novel biosensors.

MATERIAL AND METHODS

Animal Models

All studies involving mice were performed with the approval of Albert Einstein College of Medicine's Institutional Animal Care and Use Committee (IACUC). At least ten mice were studied for each condition described.

Syngeneic Orthotopic Allograft Model: Female wild type 129S6/SvEv mice at 12-16 weeks of age were used for orthotopic injections of mouse ATC cells.

Human ATC Orthotopic Xenograft Model: Two transgenic strains in the C57BL/6 genetic background were used for intravital imaging: Csf1r-Gal4VP16/UAS-ECFP expressing ECFP in macrophages (Ovchinnikov et al., 2008) and a VeCad-tdTomato/Csf1r-ECFP mouse expressing tdTomato in endothelia and ECFP in macrophages (Entenberg et al., 2018). Mice used for experiments were between 12-16 weeks of age.

Genetically Engineered Model (GEM): [*Pten, TP53*]$^{thyr-/-}$ mice (Antico Arciuch et al., 2011) with a Lox-STOP-Lox-GFP cassette knocked into the *Rosa26* locus were used. These mice were used at 8 months of age, when they develop palpable tumors.

Transfection of BHT101 and OCUT2 cells with mCherry Flip-GFP

pCDNA3-Flip-GFP (Casp3 cleavage seq) T2A mCherry was a gift from Xiaokun Shu (Addgene plasmid #124428) (Zhang et al., 2019). To prevent silencing and improve stability of high-level expression, the construct was re-cloned into pCDH-EF1-FHC, a gift from Richard Wood (Addgene plasmid #64874), in order to have the EF-1α promoter driving the construct (Wang et al., 2017).

293T cells were plated in antibiotic-free DMEM medium. Plasmids used were pMD2G (0.3 μg), pPAX2 (2.7 μg), and EF1α -mCherry-Flip-GFP (3 μg). Transfection was performed with Lipofectamine 2000. 16 hours later, the medium was aspirated and replaced with bovine serum albumin (BSA) enriched medium. The following day, this medium was collected, filtered and applied to BHT101 and OCUT2 cell lines in the presence of 0.8 μg/ml polybrene The next day the medium was aspirated and replaced with fresh medium. Puromycin selection was initiated with 1.5 μg/mL. After several days of selection, cells were FACS-sorted to select the population expressing the highest levels of mCherry. Cell lines were expanded in the presence of 1.5 μg/mL Puromycin.

Orthotopic Injection

Preparation of Cells: Anaplastic thyroid cancer (ATC) cells were trypsinized and counted using a Beckman Coulter Z2 Coulter Particle Counter. Cells were collected and centrifuged at 700RCF for 2 minutes, washed once with phosphate-buffered saline (PBS)

and centrifuged again at 700RCF for 2 minutes. The cells were suspended in PBS with a final concentration of approximately $1x10^5$ cells/10 μL for mouse ATC cells and $5x10^5$ cells/10 μL for human ATC cells, and kept on ice.

Injection Protocol: The mice were anesthetized with 5% isoflurane. The hair on the anterior neck was removed with a depilatory cream. Maintenance anesthesia was then kept at 2% isoflurane. The mouse was placed in the supine position with neck extended and limbs secured with paper tape. Chlorhexidine was used to sterilize the skin of the mouse. Surgical procedure as follows was adapted from Nucera et. al. (Nucera et al., 2009). Using sterile instruments, a transverse 1 cm incision was made at the level of the sternum and the skin was retracted to reveal the salivary glands. The left and right salivary glands were gently separated. The strap muscles overlying the trachea were lifted and incised revealing the tracheal rings. The thyroid lobes just lateral to either side of the trachea were visualized. 10 μL (mouse) or 20μL (human) of cell suspension were injected into the right thyroid lobe.

The salivary glands were replaced into their anatomically correct position and the skin closed with a running 4-0 nylon suture. The mouse was observed throughout recovery from anesthesia until normal behavior was restored.

Mouse cell line-derived tumors could be visualized and palpated at 7 days post-injection leading to an optimal time for window placement at 9-10 days post-injection. Human cell line-derived tumors became palpable after approximately 4 weeks, reflecting the substantially slower growth rate of human cells.

Window Passivation

The custom-made window is composed of a stainless steel frame with a central aperture that accepts a 5-mm coverslip (Entenberg et al., 2018). Proper cleaning and passivation of the windows is essential to prevent adverse immune reactions. Before implantation, windows were soaked for approximately 60 min in acetone to dissolve any residual glue from prior use. Windows were then rinsed in water and, as previously described, were passivated using an alkaline-acid-alkaline method (Coste et al. 2019). Windows were soaked for 30 min in a 5% solution of sodium hydroxide at 70 C, rinsed with deionized water, soaked in 7% citric acid solution at 55 C for 10 minutes, and rinsed with deionized water again. Windows were immersed in the sodium hydroxide solution for another 30 min and followed by a final rinse with deionized water.

Window Placement

Standardized Protocol: Mice were anesthetized with 5% isoflurane. The hair on the anterior neck was removed with a depilatory cream. Maintenance anesthesia was then kept at 2% isoflurane. The mouse was placed in the supine position with the neck extended and limbs secured with paper tape. Chlorhexidine was used to sterilize the skin. The full procedure is shown in Figure 1. Using sterile instruments, a 1 cm circular incision was made at the greatest prominence of the tumor. The salivary glands were gently dissected off of the tumor to avoid bleeding. The right salivary gland was pinned to the right side by suturing from the lateral cheek into the lateral neck space, through the salivary gland, back through

the salivary gland, and out through the cheek. This was tied down using an instrument tie. A purse-string suture was made in the skin around the open circular wound, close to the edges of the incision (≤1 mm), and a single tie was thrown to stabilize the suture. The custom-made window was placed within the opening and the suture was tightened within the groove. Several square knots were used to secure the window. In order to optimize contact between the window and the tumor, the window was lifted off the tumor and a small amount of cyanoacrylate glue was placed on the undersurface rim of the window. The window was then placed directly on the tumor with firm pressure for 10 seconds. A small amount of glue was then placed on the recessed rim. Using a suction applicator, the coverglass was quickly placed within the groove and held for 10 seconds.

Modifications to the Protocol

A. Salivary glands obstructing: In some mice, the salivary gland continued to obstruct the field of view despite the lateral pinning. In this case, we removed the obstructing salivary gland entirely by using either electrocautery or suture ligation of the gland.

B. Tumor not making adequate contact with the window: A smaller tumor, or a tumor positioned more posteriorly in the neck, can be difficult to visualize adequately with the anterior window. In this case we found it helpful to utilize a cross-stitch underneath the tumor that functions to lift the tissue and stabilize it against the window coverglass. This technique involves placing a suture through the skin at the superior aspect of the circular incision, passing it through the tumor in the cranial-caudal direction and then exiting through skin on the inferior aspect, all while leaving long tails at either end. Next, another suture is passed right-lateral through the skin to the tumor, underneath the cranial-caudal stitch, and exiting through the skin on the opposite side. These steps should be done following the placement of the purse-string suture and prior to the insertion of the window. After the window is placed and secured with the purse string suture, the cross-stitches can be manipulated to optimize contact between the tumor and the window.

C. Unanticipated Low Fluorescence during imaging of GEM mice: Placing the window in GEM mice who have not undergone prior thyroid surgery/neck dissection poses a unique challenge. Despite what appears grossly to be good contact between the tumor and the window, images can show low intensity fluorescence. The signal is attenuated by the unviolated fascial and muscle layers that envelop the tumor in a thin layer. In this case, careful dissection of the layer(s) can be done with the guidance of a fluorescent protein flashlight until the optimal intensity is reached. After the true tumor is exposed, the window placement can continue as per protocol.

Intravital Imaging

Mice were again anesthetized with 5% and maintained at 2% isoflurane. A thin fixturing plate was placed between the mouse and the outer lip of the window as previously described (Entenberg et al., 2018). The mouse was placed on the stage of a custom-built inverted two-laser multiphoton microscope equipped with both a Ti:Sapph laser and an optical parametric oscillator (OPO) (Entenberg et al., 2013), ensuring that the clear aperture of the window was placed directly above the objective lens. The fixturing plate was then taped down onto the

microscope stage. An environmental chamber was placed over the mouse to keep it at physiologic temperatures. A pulse oximeter (MouseStat for PhysioSuite, Kent Scientific) was used to monitor and ensure adequate breathing, heart rate, and oxygenation during imaging. Imaging was performed using multiphoton microscopy and obtained with 25x 1.05 NA objective lens. At the completion of imaging, the mouse was observed until it recovered from anesthesia. To equalize the brightness of CFP, GFP, and tdTomato fluorophores (which depends upon their relative expression levels) imaging was performed between 880 and 940 nm so as to preferentially excite one or the other of the fluorescent proteins. mCherry fluorescence was not excited by these wavelengths and required the use of the 1100 nm from the OPO. This was also useful to ensure that the fluorescence was indeed from the mCherry protein as opposed to autofluorescence.

Drug treatment

MCL1 (AZD5991)(Tron et al., 2018) and BCL2/XL (AZD4320)(Cidado et al., 2018) inhibitors were kindly provided by Dr. J. Cidado (Astra Zeneca). A 1μM solution of the two compounds in PBS was directly injected into the tumor area below the window.

Histology and Immunohistochemistry

Allograft tissues from 3 control and 3 WHITI-bearing mice were sectioned and stained for IBA1 and GFP. Microphotographs were analyzed to quantify $IBA1^{+}/GFP^{-}$ cells in three high-power fields/mouse.

RESULTS

Window for High-resolution Intravital Thyroid Imaging (WHITI)

In order to develop an intravital imaging protocol for orthotopic or autochthonous thyroid tumors, we built upon the experience gained while establishing a lung imaging window (Entenberg et al., 2018). The thyroid gland location, however, presents unique challenges that made necessary to implement a series of modifications of the lung window protocol. Once thyroid tumors have developed to a size of between 4 and 7 mm, the mice will be ready for the implantation of the WHITI.

The most salient steps in the WHITI placement are depicted in Figure 1. The anterior neck area must be carefully depilated prior to sterilizing the skin (Figure 1A). Microscopic hairs can easily get trapped underneath the window during placement, thus creating unnecessary artifacts over the tumor tissue (Figure 1B). Mouse salivary glands are superficial, large, and anatomically, lie over the tumor. Therefore, it is necessary to completely retract them off the tumor and ensure that they are as far lateral as possible to prevent obstruction of the window (Figure 1C). After this step, it is still fairly common to have the salivary glands relax back into the clear aperture of the window. For this reason, we have found it useful to pin the salivary gland to the interior lateral space of the neck of the mouse (Figure 1D). When the glands are large relative to the size of the tumor, it may also be useful to ligate or cauterize the salivary gland at its base to completely eliminate it. When creating the purse-string suture, it is best to work on the very edge of the circular incision so that the suture insertion and exit points are within 1 mm of the cut edge of the skin (Figure 1E). In this way, the

groove of the window frame will be able to easily accommodate the skin and suture. When tying the window frame down, it is important to tie tightly enough to secure the frame without causing ischemia in the skin edge (Figure 1F). Multiple square knots should be used (3-4 should suffice for unbraided suture) to prevent loosening over time.

Given that the thyroid tumor circumferentially envelops the trachea, one of the challenges inherent to this technique is the motion artifact that arises when the animal breathes during imaging. To avoid this, we have developed two approaches. One is to apply a small amount of tacking adhesive outside of the window's clear aperture, just underneath the rim of the window frame that is in contact with the tumor tissue (Figure 1G). This thin layer of glue is ideal for larger tumors where the entire window frame is in contact with the tumor rather than with surrounding tissue. The second approach, useful for smaller thyroid tumors, is the cross-stitch, a reliable technique that serves both to bring the smaller, more recessed tumor into the window's clear aperture, and to stably affix the tumor to the coverglass. This is described in further detail in the Methods section.

As with any surgical procedure, particularly those involving inflamed cancer tissue, bleeding can occur at any step. In our experience, this happens in less than 10% of the implantations. Firm digital pressure is often enough to stop an active hemorrhage, however even light serosanguinous drainage between the tumor and the window can strongly absorb pulsed multiphoton excitation light and make it more difficult to visualize the cells. Thus, the most important points to keep in mind when placing the coverglass is that the tumor and surrounding area are clean and dry. Care should be taken to remove any visible hair or fibers and irrigate with PBS if it is suspected that small particles may obstruct the view. The rim of the window frame should also be clean and dry. An insulin syringe containing adhesive can be used to place small drops of adhesive in all four quadrants of the rim followed by immediately placing the frame in contact with the tumor. This should be held in place for ~30 seconds. Finally, the lip of the window frame's inner bore should be coated with adhesive and a coverglass inserted using a vacuum applicator (Figure 1H).

Upon recovery from anesthesia, the mice are able to move and feed without impediment (not shown), as previously shown for the lung window implantation model (Entenberg et al., 2018).

Intravital imaging

Our first proof-of-principle application of the WHITI technique was the visualization of GFP-tagged murine anaplastic thyroid cancer cells. N794 cells were implanted in syngeneic 129S6/SvEv mice. Since this is a fast-growing cell line, tumors were ready to be imaged 11 days post-implantation (Figure 2A). Tightly packed spindle-shaped GFP positive cells can be seen with single-cell resolution (Figure 2A, A'). Within the mass of N794 cells, there are clearly visible black spaces suggesting the presence of other (host) cell types within the tumor. At the periphery, collagen I fibers can be seen in blue due to their ability to generate second harmonic signals.

Next, we implanted the same cells into *Rag2*$^{-/-}$ mice expressing tdTomato in endothelial cells and ECFP in macrophages. The use of this strain allows the detailed visualization of

cell-cell relationships between the implanted cells and the host. At a more superficial level, macrophages can be seen in the tumor mass with vasculature localized at the periphery (Figure 2B). Imaging of the tumor at a location several microns deeper showed vessels within the tumor, indicating that neo-vascularization is taking place (Figure 2C. C'). Time lapse imaging shows that the majority of macrophages are stationary with only a few showing any motility (Movies 1 & 2).

To visualize autochthonous tumors developing in genetically engineered mouse models of thyroid cancer, we used the [*Pten*, *Tp53*]$^{thyr-/-}$ mouse strain (Antico Arciuch et al., 2011), carrying a *Lox-STOP-Lox-GFP* cassette knocked-in into the *Rosa26* locus, which allows Cre-directed tracing of thyroid epithelial cells.

The imaging window was placed in an 8-month old [*Pten*, *Tp53*]$^{thyr-/-}$ mouse. At this age, this strain invariably develops well-differentiated follicular carcinomas (FTC) that will subsequently progress to anaplastic carcinomas (Antico Arciuch et al., 2011). Images obtained through the WHITI show a tissue organization quite distinct from the orthotopic xenograft model (Figure 2D-F). While orthotopically injected N794 ATC cells appear as disarranged sheets of spindle-like cells, the FTC imaged in the GEM model, at this age, retains the thyroid architecture, with acellular follicles seen as black spaces between the more solid tumor areas (Figure 2D-F, D').

Live imaging of apoptosis

Having successfully established the WHITI technique in different ATC mouse models, we next tested whether intravital imaging could be used to visualize and study drug effects in vivo. Real time analysis at the single cell level of the response of tumor tissue to drug-treatment would allow rapid fine-tuning of the scheduling and dosing strategies, and also offer a unique view of the changes induced over time by drug treatment in the tumor microenvironment composition and behavior. Thus, we decided to focus on the induction of tumor cell apoptosis via inhibition of BCL2 family members. Solid tumors often depend on two or more BCL2 family members for survival, with BCL-XL and MCL1 playing a prominent role in many cases (Nangia et al., 2018).

We generated two human ATC cell lines, BHT101 and OCUT2, engineered to express an apoptosis biosensor (Zhang et al., 2019). Cells were transduced with a construct constitutively expressing mCherry (as a tracer) and an inactive GFP (Flip-GFP) that can be refolded into a fluorescent protein upon Caspase 3-mediated cleavage of a target sequence inserted into the GFP coding frame (Zhang et al., 2019). After the biosensor activity was confirmed in vitro by co-treating cells with two novel MCL1 (AZD5991) (Tron et al., 2018) and BCL2/XL (AZD4320) (Cidado et al., 2018) inhibitors, both currently in clinical trials (Figure 3A), cells were injected into *Rag2*$^{-/-}$ mice expressing ECFP in macrophages. These human ATC cell lines took approximately 4 weeks to establish grossly palpable tumors adequate for visualization, at which point the WHITI was implanted. The mCherry-positive tumor was easily detected via intravital imaging (Figure 3B).

We tested the ability of the WHITI to visualize ongoing apoptosis in living mice. Simultaneous inhibition of MCL1 and BCL-XL is not feasible in vivo, since combination

treatment with BCL-XL and MCL1 inhibitors in mice at therapeutic doses results in lethal liver toxicity (Weeden et al., 2018). Thus, we decided to administer the BCL-XL and MCL1 inhibitors via local intratumoral injection. BCL-XL and MCL1 inhibitors (1μM each), dissolved in sterile PBS, were injected into the tumor area below the imaging window and the mouse was then imaged for several hours. Prior to imaging, mCherry-positive cells could be readily seen, intermingled with cyan-labeled macrophages, while no GFP fluorescence was visible (Figure 4A, A'). Four hours after treatment, there was clear GFP signal developing in the tumor (Figure 4B, B'), and six hours after treatment the GFP signal was very strong, indicating massive caspase-dependent apoptosis (Figure 4C, C').

Timing of window implantation and mouse survival

The timing of WHITI implantation, the duration of imaging, and the mouse survival for repeated imaging sessions are primarily affected by the tumor cell type. Murine ATC-carrying mice can have a window placed at 9-11 days post-tumor implantation. Imaging using this window can be performed for 24-48 hours after imaging and the mouse will typically survive until 48-72 hours post-implantation. Human ATC-carrying mice can have a window placed at 28-32 days post-tumor implantation. Imaging using this window can be performed for 24-72 hours after implantation and the mouse will typically survive for 3 to 5 days post-implantation.

The optimal time of window placement for GEM models depends largely on the timing of tumor development in that strain. The ideal time of window implantation is when a tumor is grossly palpable. Imaging using this window can be performed for 24-48 hours after imaging and the mouse will typically survive until 48-72 hours post-implantation.

Inflammatory response to WHITI implantation

To determine the possible pro-inflammatory effect of surgery and implantation of the WHITI, we analyzed sections of orthotopic N794 mouse ATC allograft tissue stained with IBA1, a general marker of macrophages. As shown in Figure 5, we did not observe any statistically significant increase in macrophages in allografts subjected to window implantation.

DISCUSSION

Intravital imaging and multiphoton microscopy have been used extensively and to great effect in studying cancer biology, in particular breast cancer (Bonapace et al., 2012, Ghaffari et al., 2019, Patsialou et al., 2013). This technology has moved the field beyond cell and tissue culture and into a more complex living system that closely recapitulates human disease. Intravital imaging has also been successfully utilized in lymph node, pancreas, liver, and kidney diseases (Hato et al., 2018).

The nature of the biological processes that can be studied has also tremendously expanded. Single cell resolution imaging has made it possible to study the cell-cell and protein interactions that are critical to the pathology of cancer as well as the effect of treatment in the live animals (Li et al., 2019).

The past several years has also seen many advancements in the development of novel biologics to combat a variety of malignancies. However, preclinical models used to study the tumor response to these compounds often fall short in terms of predicting drug effect in clinical trials. We set out to develop a novel technique to acquire more information on tumor biology and drug effects in vivo, specifically in advanced thyroid cancer.

Building on our prior experience in using surgical engineering to develop technologies to study metastasis in secondary organs (Entenberg et al., 2018, Entenberg et al., 2017, Das et al., 2013), we have developed a surgically implantable Window for High-resolution Intravital Thyroid Imaging (WHITI). This technique allows live detection of important architectural characteristics of the thyroid tumors we have studied. We are able to visualize how orthotopically implanted tumors lack any tissue organization, while genetically engineered FTC tumor models retain some native thyroid structures. In addition, the tumor mass in the orthotopic model shows an abundance of macrophages and displays elements of neovascularization. We have shown that this model can be used with a biosensor to visualize drug effects in vivo, as seen with our pro-apoptotic compounds causing caspase-dependent fluorescence. Ultimately, the key advantage of this method over studies of explanted or post-mortem tissues is its ability to track changes over time in a living animal.

While the WHITI can be an important tool in studying aggressive thyroid tumors, the technique has some limitations that will require further work. The most critical of these is the limited timespan in which the tumor can be studied, when compared to tumors in other solid organs. Thyroid tumors locally advanced enough to be able to be imaged well are also prone to causing symptoms of tracheal compression in the mouse. The addition of a solid window at the anterior surface only hastens the process. We found that there is a trade-off between opting to place the window at the time when the tumor can best be visualized and compromising the survival and thus the usefulness of the mouse. In contrast, smaller tumors may offer a smaller overall area at the initial time of imaging, however the mouse can typically survive and remain healthy for several days. Future versions of the window design may alleviate this through the use of a flexible “coverglass” that could expand with increased tumoral pressure (Tabuchi et al., 2008).

This technique represents now a unique platform for the downstream development of a variety of dedicated approaches interrogating different aspects of thyroid cancer biology. An immediate application will be its implementation to evaluate the tumor microenvironment behavior and its changes in response to drug therapies (Ferrari et al., 2019). Our ability to co-visualize tumor cells, endothelial cells, and macrophages, supports the feasibility of these approaches.

Furthermore, biosensors developed to elucidate ERK signaling pathways can be adapted to study thyroid cancers that are known to be driven by RAS-ERK in vivo (de la Cova et al., 2017, Zaballos et al., 2019).

In conclusion, intravital imaging provides a unique opportunity to study thyroid cancer not only as a cellular process, but also as a system of integrated parts within a living animal,

representing an invaluable tool to further elucidate mechanisms governing thyroid cancer biology.

Supplementary Material

Refer to Web version on PubMed Central for supplementary material.

ACKNOWLEDGEMENTS

Research reported in this publication was supported by NIH grants CA128943 and CA216248, and by a Ruth L. Kirschstein T32 Training Grant of Surgeons for the Study of the Tumor Microenvironment (CA200561). We acknowledge the Animal Housing Core Facility of Albert Einstein College of Medicine, which is partially supported by the NIH Cancer Center Support Grant to the Albert Einstein Cancer Center (P30CA013330), Einstein's Gruss-Lipper Biophotonics Center and its associated Integrated Imaging Program, and Jane A. and Myles P. Dempsey for philanthropic donations.

REFERENCES

Antico Arciuch VG, Russo MA, Dima M, Kang KS, Dasrath F, Liao XH, Refetoff S, Montagna C & Di Cristofano A 2011 Thyrocyte-specific inactivation of p53 and Pten results in anaplastic thyroid carcinomas faithfully recapitulating human tumors. Oncotarget, 2, 1109–26. [PubMed: 22190384]

Baudino TA 2015 Targeted Cancer Therapy: The Next Generation of Cancer Treatment. Curr Drug Discov Technol, 12, 3–20. [PubMed: 26033233]

Bonapace L, Wyckoff J, Oertner T, Van Rheenen J, Junt T & Bentires-Alj M 2012 If you don't look, you won't see: intravital multiphoton imaging of primary and metastatic breast cancer. J Mammary Gland Biol Neoplasia, 17, 125–9. [PubMed: 22581273]

Chen Z, Ross JL & Hambardzumyan D 2019 Intravital 2-photon imaging reveals distinct morphology and infiltrative properties of glioblastoma-associated macrophages. Proc Natl Acad Sci U S A, 116, 14254–14259. [PubMed: 31235603]

Cidado J, Secrist JP, Gibbons FD, Hennessy EJ, Ioannidis S & Clark EA 2018 AZD4320 is a potent, dual Bcl-2/xLinhibitor that rapidly induces apoptosis in preclinical hematologic tumor models. Cancer Research, 78, 311–311.

Conway JRW, Warren SC, Herrmann D, Murphy KJ, Cazet AS, Vennin C, Shearer RF, Killen MJ, Magenau A, Melenec P, Pinese M, Nobis M, Zaratzian A, Boulghourjian A, Da Silva AM, Del Monte-Nieto G, Adam ASA, Harvey RP, Haigh JJ, Wang Y, Croucher DR, Sansom OJ, Pajic M, Caldon CE, Morton JP & Timpson P 2018 Intravital Imaging to Monitor Therapeutic Response in Moving Hypoxic Regions Resistant to PI3K Pathway Targeting in Pancreatic Cancer. Cell Rep, 23, 3312–3326. [PubMed: 29898401]

Coste A, Oktay MH, Condeelis JS & Entenberg D 2019 Intravital Imaging Techniques for Biomedical and Clinical Research. Cytometry A.

Das S, Sarrou E, Podgrabinska S, Cassella M, Mungamuri SK, Feirt N, Gordon R, Nagi CS, Wang Y, Entenberg D, Condeelis J & Skobe M 2013 Tumor cell entry into the lymph node is controlled by CCL1 chemokine expressed by lymph node lymphatic sinuses. J Exp Med, 210, 1509–28. [PubMed: 23878309]

De La Cova C, Townley R, Regot S & Greenwald I 2017 A Real-Time Biosensor for ERK Activity Reveals Signaling Dynamics during C. elegans Cell Fate Specification. Dev Cell, 42, 542–553 e4. [PubMed: 28826819]

Entenberg D, Kedrin D, Wyckoff J, Sahai E, Condeelis J & Segall JE 2013 Imaging tumor cell movement in vivo. Curr Protoc Cell Biol.

Entenberg D, Pastoriza JM, Oktay MH, Voiculescu S, Wang Y, Sosa MS, Aguirre-Ghiso J & Condeelis J 2017 Time-lapsed, large-volume, high-resolution intravital imaging for tissue-wide analysis of single cell dynamics. Methods, 128, 65–77. [PubMed: 28911733]

Entenberg D, Voiculescu S, Guo P, Borriello L, Wang Y, Karagiannis GS, Jones J, Baccay F, Oktay M & Condeelis J 2018 A permanent window for the murine lung enables high-resolution imaging of cancer metastasis. Nat Methods, 15, 73–80. [PubMed: 29176592]

Ferrari SM, Fallahi P, Galdiero MR, Ruffilli I, Elia G, Ragusa F, Paparo SR, Patrizio A, Mazzi V, Varricchi G, Marone G & Antonelli A 2019 Immune and Inflammatory Cells in Thyroid Cancer Microenvironment. Int J Mol Sci, 20.

Ghaffari A, Hoskin V, Turashvili G, Varma S, Mewburn J, Mullins G, Greer PA, Kiefer F, Day AG, Madarnas Y, Sengupta S & Elliott BE 2019 Intravital imaging reveals systemic ezrin inhibition impedes cancer cell migration and lymph node metastasis in breast cancer. Breast Cancer Res, 21, 12. [PubMed: 30678714]

Gyarmati G, Kadoya H, Moon JY, Burford JL, Ahmadi N, Gill IS, Hong YK, Der B & Peti-Peterdi J 2018 Advances in Renal Cell Imaging. Semin Nephrol, 38, 52–62. [PubMed: 29291762]

Hato T, Winfree S & Dagher PC 2018 Kidney Imaging: Intravital Microscopy. Methods Mol Biol, 1763, 129–136. [PubMed: 29476494]

Hui L & Chen Y 2015 Tumor microenvironment: Sanctuary of the devil. Cancer Lett, 368, 7–13. [PubMed: 26276713]

Junankar S, Shay G, Jurczyluk J, Ali N, Down J, Pocock N, Parker A, Nguyen A, Sun S, Kashemirov B, Mckenna CE, Croucher PI, Swarbrick A, Weilbaecher K, Phan TG & Rogers MJ 2015 Real-time intravital imaging establishes tumor-associated macrophages as the extraskeletal target of bisphosphonate action in cancer. Cancer Discov, 5, 35–42. [PubMed: 25312016]

Ke CC, Liu RS, Suetsugu A, Kimura H, Ho JH, Lee OK & Hoffman RM 2013 In vivo fluorescence imaging reveals the promotion of mammary tumorigenesis by mesenchymal stromal cells. PLoS One, 8, e69658. [PubMed: 23936067]

Landa I, Ibrahimpasic T, Boucai L, Sinha R, Knauf JA, Shah RH, Dogan S, Ricarte-Filho JC, Krishnamoorthy GP, Xu B, Schultz N, Berger MF, Sander C, Taylor BS, Ghossein R, Ganly I & Fagin JA 2016 Genomic and transcriptomic hallmarks of poorly differentiated and anaplastic thyroid cancers. J Clin Invest, 126, 1052–66. [PubMed: 26878173]

Lehmann C, Fisher NB, Tugwell B & Zhou J 2016 An intravital microscopy model to study early pancreatic inflammation in type 1 diabetes in NOD mice. Intravital, 5, e1215789. [PubMed: 28243521]

Li R, Attari A, Prytyskach M, Garlin MA, Weissleder R & Miller MA 2019 Single-Cell Intravital Microscopy of Trastuzumab Quantifies Heterogeneous in vivo Kinetics. Cytometry A.

Malehmir M, Pfister D, Gallage S, Szydlowska M, Inverso D, Kotsiliti E, Leone V, Peiseler M, Surewaard BGJ, Rath D, Ali A, Wolf MJ, Drescher H, Healy ME, Dauch D, Kroy D, Krenkel O, Kohlhepp M, Engleitner T, Olkus A, Sijmonsma T, Volz J, Deppermann C, Stegner D, Helbling P, Nombela-Arrieta C, Rafiei A, Hinterleitner M, Rall M, Baku F, Borst O, Wilson CL, Leslie J, O'connor T, Weston CJ, Adams DH, Sheriff L, Teijeiro A, Prinz M, Bogeska R, Anstee N, Bongers MN, Notohamiprodjo M, Geisler T, Withers DJ, Ware J, Mann DA, Augustin HG, Vegiopoulos A, Milsom MD, Rose AJ, Lalor PF, Llovet JM, Pinyol R, Tacke F, Rad R, Matter M, Djouder N, Kubes P, Knolle PA, Unger K, Zender L, Nieswandt B, Gawaz M, Weber A & Heikenwalder M 2019 Platelet GPIbalpha is a mediator and potential interventional target for NASH and subsequent liver cancer. Nat Med, 25, 641–655. [PubMed: 30936549]

Nangia V, Siddiqui FM, Caenepeel S, Timonina D, Bilton SJ, Phan N, Gomez-Caraballo M, Archibald HL, Li C, Fraser C, Rigas D, Vajda K, Ferris LA, Lanuti M, Wright CD, Raskin KA, Cahill DP, Shin JH, Keyes C, Sequist LV, Piotrowska Z, Farago AF, Azzoli CG, Gainor JF, Sarosiek KA, Brown SP, Coxon A, Benes CH, Hughes PE & Hata AN 2018 Exploiting MCL1 Dependency with Combination MEK + MCL1 Inhibitors Leads to Induction of Apoptosis and Tumor Regression in KRAS-Mutant Non-Small Cell Lung Cancer. Cancer Discov, 8, 1598–1613. [PubMed: 30254092]

Nucera Carmelo, Nehs Matthew, A., Mekel Michal, Zhang Xuefeng, Hodin Richard, Lawler Jack, Nose Vania, Parangi Sareh 2009 A novel orthotopic mouse model of human anaplastic thyroid carcinoma. Thyroid, 19, 1077–84. [PubMed: 19772429]

Ovchinnikov DA, Van Zuylen WJ, Debats CE, Alexander KA, Kellie S & Hume DA 2008 Expression of Gal4-dependent transgenes in cells of the mononuclear phagocyte system labeled with enhanced cyan fluorescent protein using Csf1r-Gal4VP16/UAS-ECFP double-transgenic mice. J Leukoc Biol, 83, 430–3. [PubMed: 17971498]

Patsialou A, Bravo-Cordero JJ, Wang Y, Entenberg D, Liu H, Clarke M & Condeelis JS 2013 Intravital multiphoton imaging reveals multicellular streaming as a crucial component of in vivo cell migration in human breast tumors. Intravital, 2, e25294. [PubMed: 25013744]

Ritsma L, Steller EJ, Beerling E, Loomans CJ, Zomer A, Gerlach C, Vrisekoop N, Seinstra D, Van Gurp L, Schafer R, Raats DA, De Graaff A, Schumacher TN, De Koning EJ, Rinkes IH, Kranenburg O & Van Rheenen J 2012 Intravital microscopy through an abdominal imaging window reveals a pre-micrometastasis stage during liver metastasis. Sci Transl Med, 4, 158ra145.

Saeidnia S, Manayi A & Abdollahi M 2015 From in vitro Experiments to in vivo and Clinical Studies; Pros and Cons. Curr Drug Discov Technol, 12, 218–24. [PubMed: 26778084]

Saini S, Tulla K, Maker AV, Burman KD & Prabhakar BS 2018 Therapeutic advances in anaplastic thyroid cancer: a current perspective. Mol Cancer, 17, 154. [PubMed: 30352606]

Schaefer C, Schroeder M, Fuhrhop I, Viezens L, Otten J, Fiedler W, Ruther W & Hansen-Algenstaedt N 2011 Primary tumor dependent inhibition of tumor growth, angiogenesis, and perfusion of secondary breast cancer in bone. J Orthop Res, 29, 1251–8. [PubMed: 21381098]

Tabuchi A, Mertens M, Kuppe H, Pries AR & Kuebler WM 2008 Intravital microscopy of the murine pulmonary microcirculation. J Appl Physiol, 104, 338–46. [PubMed: 18006870]

Tron AE, Belmonte MA, Adam A, Aquila BM, Boise LH, Chiarparin E, Cidado J, Embrey KJ, Gangl E, Gibbons FD, Gregory GP, Hargreaves D, Hendricks JA, Johannes JW, Johnstone RW, Kazmirski SL, Kettle JG, Lamb ML, Matulis SM, Nooka AK, Packer MJ, Peng B, Rawlins PB, Robbins DW, Schuller AG, Su N, Yang W, Ye Q, Zheng X, Secrist JP, Clark EA, Wilson DM, Fawell SE & Hird AW 2018 Discovery of Mcl-1-specific inhibitor AZD5991 and preclinical activity in multiple myeloma and acute myeloid leukemia. Nat Commun, 9, 5341. [PubMed: 30559424]

Vennin C, Chin VT, Warren SC, Lucas MC, Herrmann D, Magenau A, Melenec P, Walters SN, Del Monte-Nieto G, Conway JR, Nobis M, Allam AH, Mccloy RA, Currey N, Pinese M, Boulghourjian A, Zaratzian A, Adam AA, Heu C, Nagrial AM, Chou A, Steinmann A, Drury A, Froio D, Giry-Laterriere M, Harris NL, Phan T, Jain R, Weninger W, Mcghee EJ, Whan R, Johns AL, Samra JS, Chantrill L, Gill AJ, Kohonen-Corish M, Harvey RP, Biankin AV, Australian Pancreatic Cancer Genome, I., Evans TR, Anderson KI, Grey ST, Ormandy CJ, Gallego-Ortega D, Wang Y, Samuel MS, Sansom OJ, Burgess A, Cox TR, Morton JP, Pajic M & Timpson P 2017 Transient tissue priming via ROCK inhibition uncouples pancreatic cancer progression, sensitivity to chemotherapy, and metastasis. Sci Transl Med, 9.

Wang X, Xu Z, Tian Z, Zhang X, Xu D, Li Q, Zhang J & Wang T 2017 The EF-1alpha promoter maintains high-level transgene expression from episomal vectors in transfected CHO-K1 cells. J Cell Mol Med, 21, 3044–3054. [PubMed: 28557288]

Weeden CE, Ah-Cann C, Holik AZ, Pasquet J, Garnier JM, Merino D, Lessene G & Asselin-Labat ML 2018 Dual inhibition of BCL-XL and MCL-1 is required to induce tumour regression in lung squamous cell carcinomas sensitive to FGFR inhibition. Oncogene, 37, 4475–4488. [PubMed: 29743589]

Wu T & Dai Y 2017 Tumor microenvironment and therapeutic response. Cancer Lett, 387, 61–68. [PubMed: 26845449]

Xu B, Fuchs TL, Dogan S, Landa I, Katabi N, Fagin JA, Tuttle RM, Sherman EJ, Gill AJ & Ghossein RM 2020 Dissecting Anaplastic Thyroid Carcinoma (ATC): A Comprehensive Clinical, histologic, Immunophenotypic, and Molecular Study of 360 Cases. Thyroid.

Zaballos MA, Acuna-Ruiz A, Morante M, Crespo P & Santisteban P 2019 Regulators of the RAS-ERK pathway as therapeutic targets in thyroid cancer. Endocr Relat Cancer, 26, R319–R344. [PubMed: 30978703]

Zhang Q, Schepis A, Huang H, Yang J, Ma W, Torra J, Zhang SQ, Yang L, Wu H, Nonell S, Dong Z, Kornberg TB, Coughlin SR & Shu X 2019 Designing a Green Fluorogenic Protease Reporter by Flipping a Beta Strand of GFP for Imaging Apoptosis in Animals. J Am Chem Soc, 141, 4526–4530. [PubMed: 30821975]

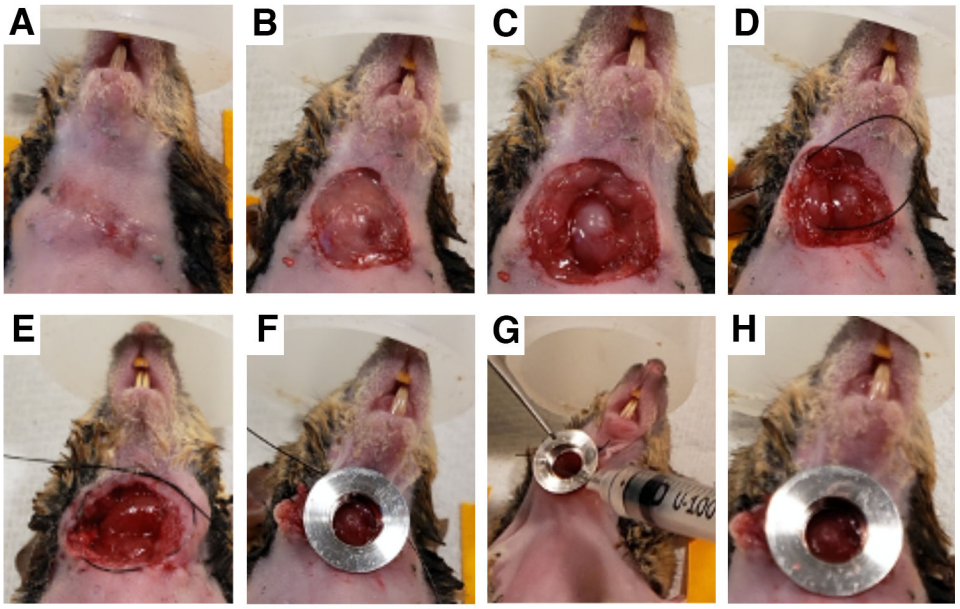

Figure 1.

Surgical implantation of the thyroid window. **A**, the hair on the anterior neck of the mouse is removed and the skin is sterilized with chlorhexidine. **B**, tumor exposure: a small circular incision is made over the palpable tumor. **C**, the salivary glands are gently retracted, exposing the tumor. **D**, the obstructing salivary gland is pinned to the skin. **E**, a circumferential purse-string suture is made around the open area. **F**, the window frame is placed into the incision and the purse-string suture tightened and tied. **G**, the window frame is gently lifted, tacking adhesive is applied to its underside, and the frame is placed in contact with the tumor, holding firm pressure for ~30 seconds. **H**, a small amount of adhesive is applied on the lower lip of the window frame bore, and the coverslip is placed inside sealing the neck space.

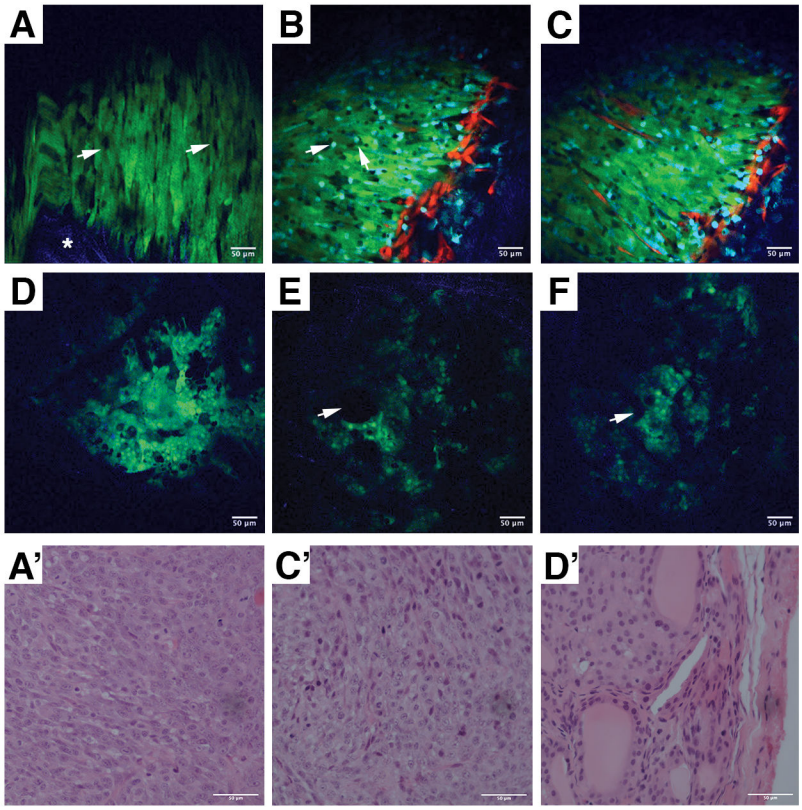

Figure 2.

Intravital imaging of mouse-derived ATC allografts, xenografts, and GEM models. **A**, N794 cells orthotopically injected into the right thyroid lobe of a syngeneic 129S6/SvEv mice. The window was implanted 11 days after tumor grafting. Arrowheads indicate infiltrating host cells, while the asterisk indicates the collagen I fibers. **A'**, H&E staining of the tumor shown in A. **B-C**, N794 cells orthotopically injected into the right thyroid lobe of a *Rag2*$^{-/-}$ Mac-blue/ve-cadherin tdTomato mouse. The window was implanted 11 days after grafting. **B**, cyan macrophages (arrows) infiltrate the tumor. **C**, red vessels at a deeper level within the tumor show neovascularization. **C'**, H&E staining of the tumor shown in B-C. **D-F**, Intravital imaging of an 8-month old [*Pten*, *Tp53*]$^{thyr-/-}$ mouse expressing GFP as a thyroid tracer. **D**, organized tissue architecture can be observed, distinguishing the well-differentiated tumor model from the orthotopic ATC implantation model. **E**, **F** large black spaces (arrowheads) correspond to thyroid follicles and blue collagen fibers can be seen within the tumor, providing structural support. **D'**, H&E staining of the tumor shown in D-F. Green = GFP^{+} tumor cells, Red = tdTomato^{+} endothelia, Blue = Second harmonic generation from collagen I fibers, Cyan = CFP^{+} macrophages.

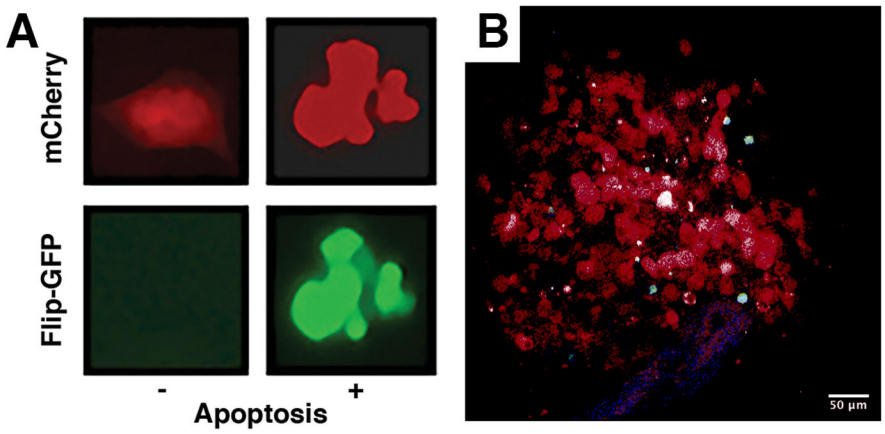

Figure 3.

Characterization of the apoptosis biosensor in OCUT2 human anaplastic thyroid cancer (ATC) cells. A, in vitro imaging demonstrating constitutive mCherry expression in cells exposed to either control or pro-apoptotic treatment, and GFP fluorescence in the presence of pro-apoptotic treatment. B, OCUT2 cells orthotopically injected into a $Rag2^{-/-}$ mouse. Window implanted and intravital images taken 4 weeks post-injection.

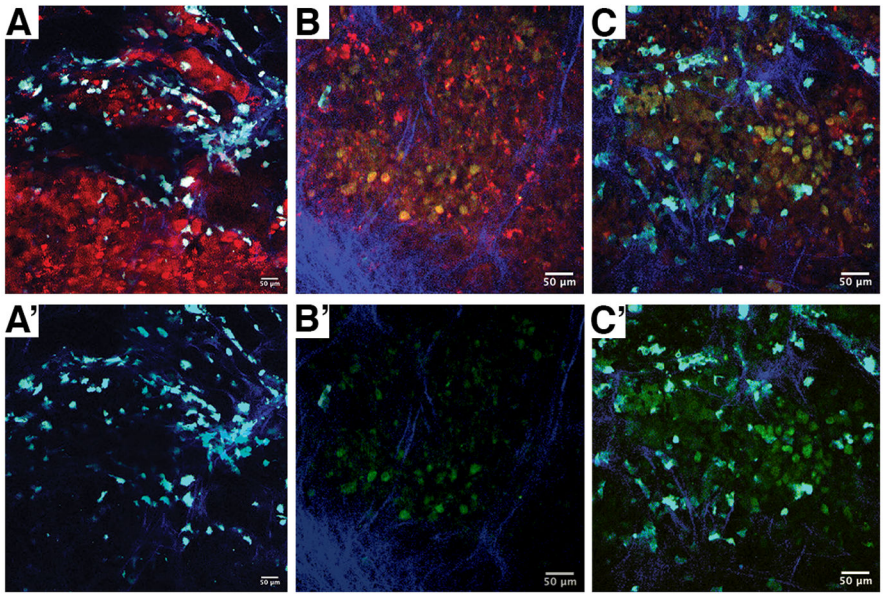

Figure 4.

Time course of apoptosis induction in an OCUT2 tumor orthotopically grafted in a Rag2$^{-/-}$ Mac-blue mouse. A, pretreatment image demonstrating mCherry^{+} cells without appreciable GFP signal. Following acquisition of pretreatment images, the tumor was injected with 1 μM of BCL-XL and MCL1 inhibitors. B, 4 hours post-treatment, mCherry^{+} and GFP^{+} double-positive cells can be seen, indicating caspase-dependent apoptosis. **C**, the GFP signal intensifies at six hours post treatment, indicating massive apoptosis. **A', B'** and **C'** are the respective images with the mCherry signal removed to more easily appreciate the GFP signal.

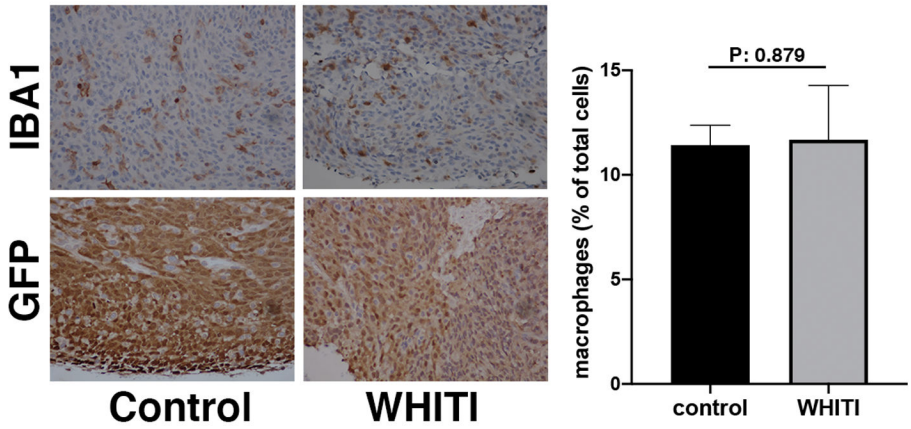

Figure 5.

A-D, Representative GFP (thyroid cells)- and IBA1 (macrophages)-stained sections from N794 syngeneic allografts untouched (**A**, **B**) or three days after window implantation (**C**, **D**). **E**, graph showing the of the occurrence of infiltrating macrophages in the two conditions.